In-situ observation of pre-, co- and post-seismic shear slip at 1.5 km depth

Martin Schoenball[1], Yves Guglielmi[1], Jonathan Blair Ajo-Franklin[2], Paul J Cook[3], Patrick Dobson[4], Chet Hopp[1], Timothy J Kneafsey[5], Florian Soom[1], and Craig Ulrich[6]

[1]Lawrence Berkeley National Laboratory
[2]Rice University
[3]LBNL
[4]Lawrence Berkeley National Laboratory (DOE)
[5]Lawrence Berkeley Laboratory
[6]Lawerence Berkeley National Laboratory

November 26, 2022

Abstract

Understanding the initiation and arrest of earthquakes is one of the long-standing challenges of seismology. Here we report on direct observations of borehole displacement by a meter-sized shear rupture induced by pressurization of metamorphic rock at 1.5 km depth. We observed the acceleration of sliding, followed by fast co-seismic slip and transient afterslip. Total displacements were about 7, 5.5 and 9.5 micrometers, respectively for the observed pre-slip, co-seismic slip and afterslip. The observed pre-slip lasted about 0.4 seconds. Co-seismic slip was recorded by the 1 kHz displacement recording and a 12-component array of 3-C accelerometers sampled at 100 kHz. The observed afterslip is consistent with analytical models of arrest in a velocity-strengthening region and subsequent stress relaxation.

The observed slip vector agrees with the activation of a bedding plane within the phyllite, which is corroborated by relocated seismic events that were observed during the later stages of the injection experiment.

In-situ observation of pre-, co- and post-seismic shear slip at 1.5 km depth

Martin Schoenball, Yves Guglielmi, Jonathan B. Ajo-Franklin, Paul Cook, Patrick F. Dobson, Chet Hopp, Timothy J. Kneafsey, Florian Soom, Craig Ulrich and EGS Collab Team

Key points:

- Direct observation of displacement from a shear rupture in crystalline rock at 1.5km depth
- Rupture was observed including transients of aseismic pre-slip, co-seismic, and afterslip phases
- Co-seismic rupture phase accounts for only 25% of total slip

Abstract

Understanding the initiation and arrest of earthquakes is one of the long-standing challenges of seismology. Here we report on direct observations of borehole displacement by a meter-sized shear rupture induced by pressurization of metamorphic rock at 1.5 km depth. We observed the acceleration of sliding, followed by fast co-seismic slip and a transient afterslip phase. Total displacements were about 7, 5.5 and 9.5 micrometers, respectively for the observed pre-slip, co-seismic slip and afterslip. The observed pre-slip lasted about 0.4 seconds. Co-seismic slip was recorded by the 1 kHz displacement recording and a 12-component array of 3-C accelerometers sampled at 100 kHz. The observed afterslip is consistent with analytical models of arrest in a velocity-strengthening region and subsequent stress relaxation.

The observed slip vector agrees with the activation of a bedding plane within the phyllite, which is corroborated by relocated seismic events that were observed during the later stages of the injection experiment.

Plane language summary

Because earthquakes typically occur at great depths, and we cannot predict when and where the next event will occur, it is very difficult to observe their beginning and their end. We instrumented a borehole in a 1.5 km deep mine with precise displacement sensors and created a meter-sized rupture through fluid injection. We were not only able to capture the fast displacement that is responsible for the ground

30 shaking associated with earthquakes, but also its slow onset and finally the decelerating until its arrest.

31 From our measurements we inferred that only about a quarter of the total displacements is associated with

32 seismic waves, while most of the displacement is slow. Further analysis revealed that the event aligned

33 with bedding planes of the host rock and not – as commonly assumed – with natural fractures.

Introduction

35 How do earthquakes start? This is a fundamental question that to date has not been answered by direct

36 observational data. Knowing how earthquakes initiate could have important implications on rapid

37 assessment of earthquakes with applications to earthquake early warning. Capturing the onset of an

38 earthquake with sensors close to the hypocenter could provide important insights towards furthering our

39 understanding of rupture initiation. However, not knowing when and where the next earthquake occurs

40 almost precludes efforts to capture the initiation of a tectonic earthquake with direct measurements.

41 Further, the depth of most earthquake hypocenters prohibits instrumenting even known repeating

42 earthquake hypocenters with in-situ sensors (Nadeau & Johnson, 1998; McGuire et al., 2005; Savage et

43 al., 2017).

44

45 Two endmember models exist that describe the onset of earthquakes and are debated in the community.

46 The first, the cascade model (Ellsworth & Beroza, 1995), is based on small ruptures coalescing into a

47 larger rupture promoted by static stress transfer. Prominent examples are observations of foreshock

48 sequences observed for the 1999 Hector Mine (Yoon et al., 2019) and Izmit (Ellsworth & Bulut, 2019)

49 earthquakes. The complementary model, the pre-slip model, argues for stable-sliding pre-slip

50 transitioning into slip-weakening behavior and reaching seismic slip speeds accompanied by seismic

51 wave radiation and ground shaking. While this model has significant theoretical support from dynamic

52 rupture modelling (Cattania & Segall, 2020 and references therein) observational support for this model is

53 sparse. Rare examples include the observation of very low frequency events accelerating into earthquakes

54 in Alaska (Tape et al., 2018) and laboratory experiments on meter-sized samples (McLaskey & Lockner,

55 2014; McLaskey, 2019).

56

57 Here we present direct observations in support of the pre-slip model from a series of meso-scale injection

58 experiments performed at 1480 m depth. Using passive seismic monitoring and in-situ displacement

59 sensors sensitive to μm-scale deformation and rotation we closely tracked the initiation of a hydraulic

60 fracture, i.e., an opening mode fracture that propagates for pore fluid pressures greater than the least

61 principal stress (Guglielmi et al., 2021). During the pressurization stage, and before the initiation of the

62 hydraulic fracture, we observed the slippage caused by a single shear event including its pre-slip, co-

63 seismic and afterslip phases. Subsequently, we will provide a brief overview of the setup of the injection

64 experiment and in-situ observations of hydraulic fracturing. We then focus on the shear event and its pre-

65 seismic, co-seismic and post-seismic phases.

66

67 ## Experimental setup and data

68 The EGS Collab project (Kneafsey et al., 2019; 2020; 2021) experimental testbeds are located in the

69 Sanford Underground Research Facility in Lead, South Dakota, which provides easy access to rock with

70 1.5 km of overburden (Heise, 2015). We established a testbed in a metamorphic rock mass comprising six

71 dedicated monitoring boreholes and two boreholes for stimulation. The monitoring boreholes are

72 equipped with a multi-modal instrument string including passive seismic sensors, active seismic sources,

73 fiber-optics for distributed sensing, and electrodes for electrical resistivity tomography. Three-

74 dimensional borehole displacements were recorded by two SIMFIP sensors (Guglielmi et al., 2014)

75 deployed in the stimulation and in the production boreholes, respectively.

76

77 Here we focus on recordings of the SIMFIP sensor installed in the borehole injection interval and of the

78 passive seismic network only. Results of other monitoring techniques and coupled modelling are

79 described in Kneafsey et al. (2019; 2020; 2021) and references therein. The SIMFIP sensor measures the

80 3-D displacements of the borehole wall across a pressurized borehole interval using seven Fiber-Bragg

81 gratings (FBG) that sense strain in six different directions of a special-designed cage and pressure. This

82 allows us to infer six degrees of displacement (three translational and three rotational) between two points

83 clamped 0.80 m apart on the borehole wall. The clamped cage sits centered but mechanically decoupled

84 in a 1.64 m long pressurized interval between two inflatable packers. The FBGs were continuously

85 sampled at 1 kHz. The six deformation sensing arms and the pressure sensor of the SIMFIP probe are

86 interrogated with a single ultra-wide wavelength-swept laser which detects the characteristic wavelength

87 of each FBG and its variation with the FBG deformation. Since these 6 strain + 1 pressure data are set on

88 two optical fibers but scanned with the same interrogator, the noise floor is correlated between FBGs. To

89 decrease the relative noise amplitude, we take the pressure channel as reference and apply a zero phase,

90 high-pass Butterworth filter with 25 Hz corner frequency to extract the noise signal. This noise channel,

91 multiplied by a scaling factor to reflect the different noise amplitudes resulting from the sensor geometry,

92 is then subtracted from each of the deformation channels. The results are the deformations without the

93 correlated noise of the interrogator laser. The deformations of the six arms can then be used to calculate

94 the six degrees of freedom of translation and rotation. Seismic activity was recorded by a network of

95 twelve 3-component accelerometers (PCB 356B18) and 24 hydrophones (High Tech HTI-96-Min),

96 continuously sampled at 100 kHz by a 24-bit digitizer (Data Translation, VibBox-64). The sensors were

97 grouted in place in six monitoring boreholes, surrounding the experimental volume in 3-D (Schoenball et
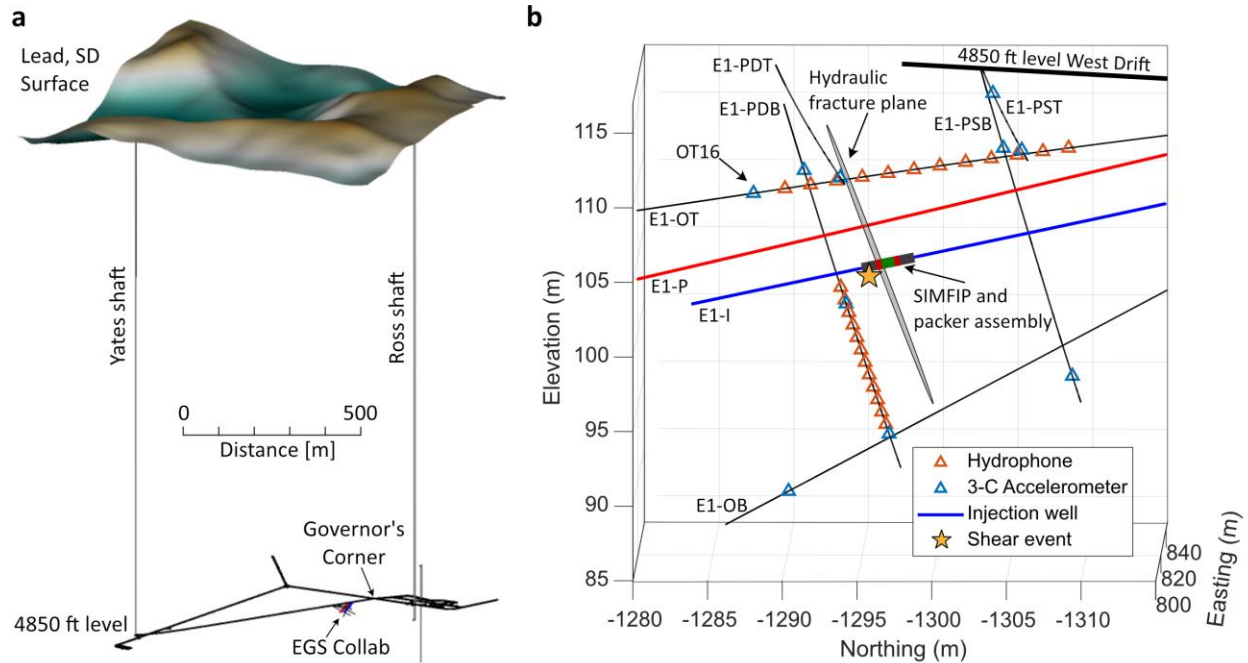98 al., 2020).

99

Figure 1: (a) Location of the EGS Collab testbed on the 4850 ft level at the Sanford Underground
Research Facility. (b) Testbed layout with monitoring and experimentation boreholes, and monitoring
system. The SIMFIP assembly is drawn to scale and colors correspond to the packers (gray), the
pressurized interval (red) and the clamped interval (green). The hydraulic fracture plane determined
from event hypocenters is indicated by the gray disk seen almost edge-on. The single shear event (yellow
star) was located just below the SIMFIP assembly.

Overview of hydraulic testing

107 The injection borehole was drilled along an azimuth of approximately N358˚E, close to the direction of
108 the least principal stress N002˚E. The hole was drilled with 96 mm diameter and left uncased beyond the
109 first 6 m. The initial injection was performed at approximately 50 m depth. A centimeter-sized notch was
110 cut into the borehole wall to guide the initiation of the hydraulic fracture. Before the experiment, optical
111 (OTV) and acoustic televiewer (ATV) logs were acquired, and a repeat ATV log was acquired after the
112 experiment, which did not reveal significant damage (Figure 2).
113 The hydraulic test was designed to create a hydraulic fracture of a nominal radius of 1.5 m. The interval
114 was pressurized by a constant injection of 200 mL/min of water. The pore fluid pressure p in the interval
115 rose linearly with time, elastically stressing the interval (Figure S1). Well before the onset of hydraulic
116 fracturing, at 21:55:11 (p = 13.4 MPa) the first seismic event was recorded. This event was accompanied

117 by significant shear displacements recorded by the SIMFIP probe (Figure 3). We will discuss this event in

118 detail below.

119 At 21:55:44 UTC (p = 20.9 MPa), the fluid pressure left the linear regime, and displacements indicated

120 the opening of a hydraulic fracture. A first pressure maximum of 24.6 MPa was reached at 21:56:08 UTC

121 (Figure S1). Pressure slowly declined until 21:56:40 UTC (p = 23.5 MPa), when it slowly increased until

122 the end of injection at 22:05:16 UTC (p = 26.3 MPa). The development of the hydraulic fracture during

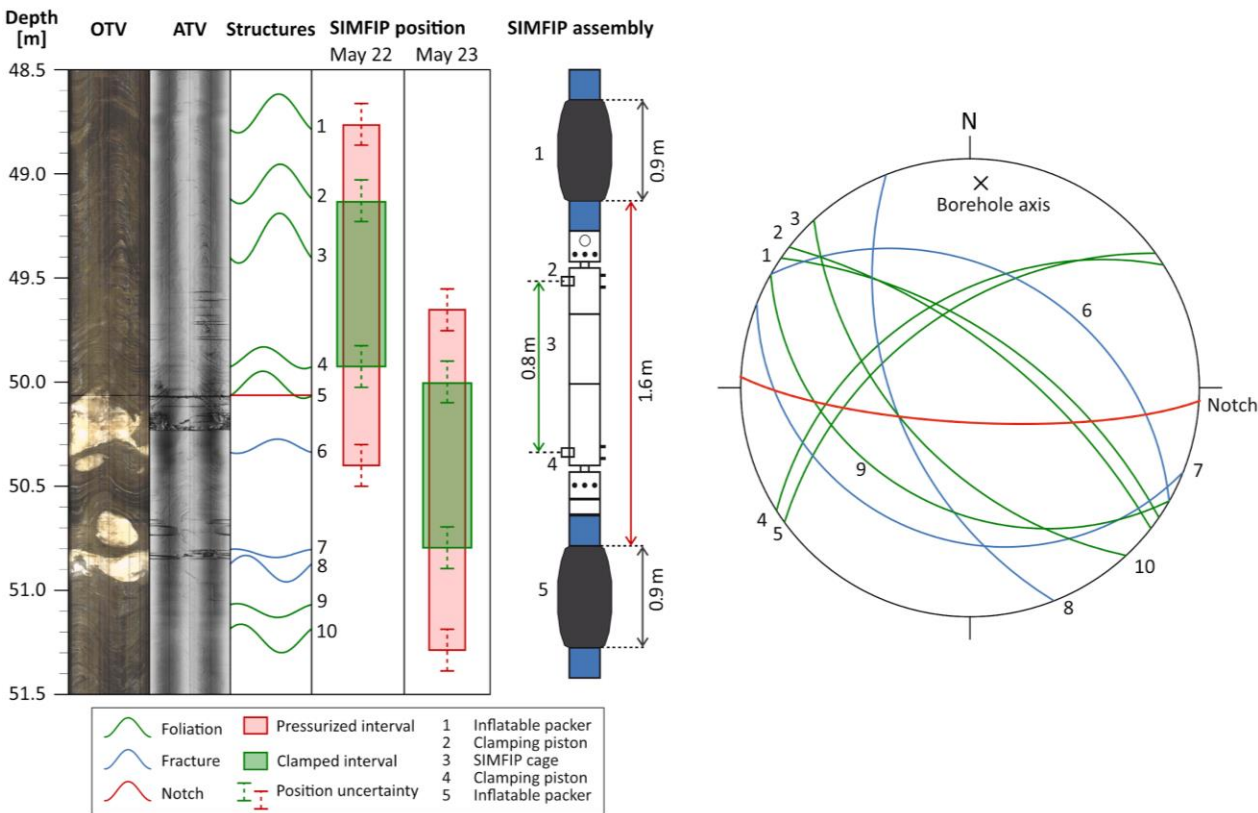123 this test and several re-opening and propagation cycles is described in Guglielmi et al. (2021).

124

125

126

127 *Figure 2: Optical and acoustic televiewer logs and structural interpretations of the borehole section of*

128 *E1-I containing the pressurized intervals. The pressurized and clamped intervals on May 22 and May 23*

129 *are drawn as red and green rectangles, respectively. The assembly containing the SIMFIP probe and*

130 *inflatable packers is shown in the middle. On the right, the foliation and fracture planes intersecting the*

131 *interval are plotted in a lower hemisphere stereo plot. The numbers correspond to the features identified*

132 *in the Structures panel.*

Early shear event

Figure 3 shows a close-up of the displacement transient related to the early shear event recorded at 21:55:11 during the injection. Due to technical problems, after each recording interval of about 3 seconds there is a gap of about 2 seconds in the data stream. The fluid pressure measured in the clamped interval was 13.4 MPa and did not show any significant deviation from its linear trend during ongoing pressurization of the packed-off interval. This indicates that no fluid leaked off from the interval as a result of the shear displacement.

We recorded displacements in borehole radial direction during the entire 3-second data segment that includes the event. No displacement was observed during the data segment before. The displacement transient therefore started during the end of a data gap and we just missed the true onset of deformation. From the beginning of the data segment, we observe linearly increasing shear displacements (pre-slip) during about 0.3 s (0.4 s if we extrapolate the linear trend to the beginning) to a total of 7 µm. Shear displacement then continues to increase by 5.5 µm during an accelerated slip event (coseismic) lasting about 0.022 s. Then, displacement decelerates in an exponential-type decay during the remainder of the data segment (afterslip). At the end of the data segment a total of 22 µm of slip had accumulated. Immediately after the coseismic slip, there may be some low frequency reverberations measured by the SIMFIP probe but the signal-to-noise ratio is too small to make a definitive observation.

Based on the 5.5 µm coseismic slip and general scaling relations of earthquakes (Kwiatek et al., 2011), we obtain a slip patch on the order of 1 m and a moment magnitude on the order of M_W −3 to −2.

During the same time period, axial displacements continue to decrease as before during the linear pressure increase. During the slip event, we observe minimal additional axial closure, which confirms that the slippage occurred just outside the clamping interval. Axial deformation during the slip event can be estimated to be less than 1 µm.

At the time of the observed shear displacement, the accelerometer array recorded a seismic event with the strongest waveforms at least until the first pressure maximum was reached at 21:56:08 UTC. It was clearly visible on all channels of the monitoring array. The waveforms (Figure 3b and Figure S2) indicate a complex rupture with at least two sub-events evidenced by two S-wave trains. Manually picked first arrivals of P and S waves were used to locate the event. We determined the hypocenter to be about 0.8 m below the injection interval (Figure 1). Given the formal location uncertainty (2-sigma) of about 1.3 m and that of the borehole trajectory of about 1 m, the event hypocenter could be within the pressurized interval as indicated by the direct measurements of displacement.
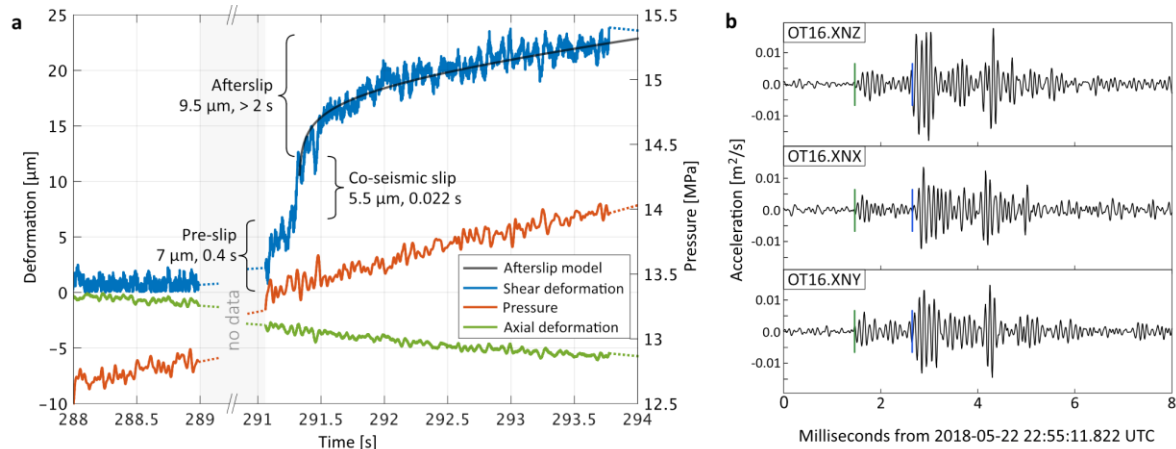
Figure 3: (a) Shear and axial displacement and injection interval pressure before, during and after the shear event. (b) Seismic waveforms of the shear event at the closest accelerometer OT16, band pass filtered between 3 and 15 kHz. P and S-wave arrivals are marked by green and blue dashes, respectively.

The goal of this experiment was to create a hydraulic fracture in an intact rock mass. Neither the optical nor the acoustic image logs indicated the presence of fractures within the selected interval for pressurization. However, the phyllite rock mass shows a pervasive fabric with bedding planes of varying orientation. In addition, it contains several quartz inclusions (lighter colored features in the OTV shown in Figure 2).

We did not observe any other discrete shear events in the pressurized interval using the SIMFIP probe during any later test at this location. In other words, although pressure was increasing to much higher levels during the later stages of hydraulic fracturing, there was no repeated activation of the same slip patch. However, additional seismic events could be located close to the injection interval. These were relocated by Chai et al. (2020) using tomoDD for joint inversion for relative locations and a 3-D velocity model. Figure 4 shows the seismicity located during the entire test together with our absolute location of the discrete shear event. We see a clear trend delineated by the hypocenters about 4 m long. We fitted planes to the hypocenters and used bootstrap resampling to evaluate the parameter space of possible planes and computed an average orientation. These, along with the slip vectors measured by the SIMFIP and the structures identified in the image logs, are plotted in Figure 4c. There is good agreement of the possible slip planes and the average plane with foliation planes 1 and 2. Further, the slip vectors also match these planes, indicating that slip initiated on a foliation plane and propagated bi-laterally, as delineated by the later seismic events. The slip vectors also coincide with the plane defined by the machined notch, indicating that it could have helped to initiate the slip event.
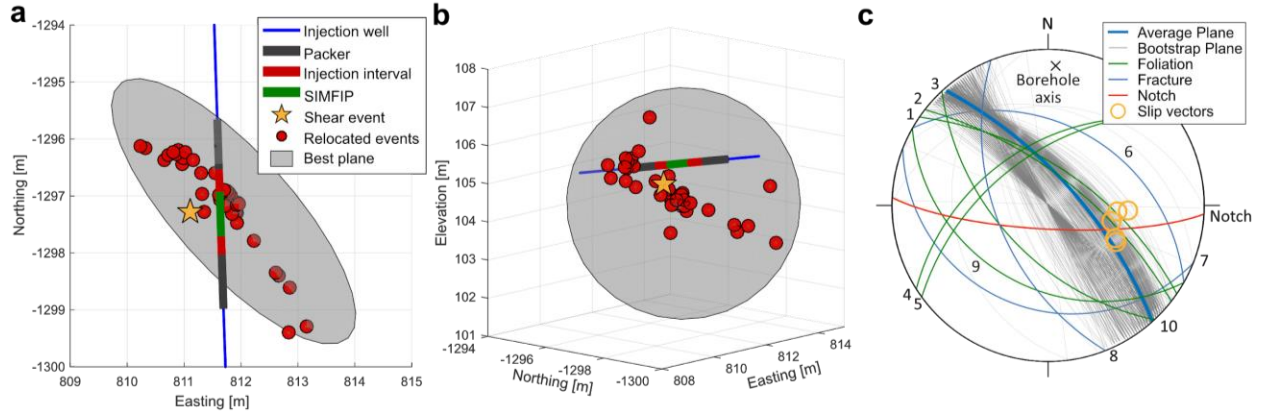
190

191 *Figure 4: (a-b) Three-dimensional view of SIMFIP assembly, the absolute location of the shear event and*
192 *relocated seismicity during the injection step. (c) Stereoplot of structures identified on image logs,*
193 *possible planes derived from hypocenters of relocated seismicity (Chai et al., 2020) with an average*
194 *plane and slip vectors for the shear event measured by the SIMFIP.*

Displacement transients

196 At the beginning of the data segment we record already about 2 μm displacement that continued to grow
197 linearly. The pre-slip we recorded lasted about 0.3 seconds with a slip speed of about 17.5 μm/s. If we
198 linearly extrapolate the onset of pre-slip into the preceding data gap we estimate the total duration of the
199 pre-slip phase to be about 0.4 s.

200 Pre-slip transients similar to ours with linearly increasing slip velocity before the transition to dynamic
201 rupture have also been observed by McLaskey & Lockner (2014) in their laboratory experiments on
202 meter-sized samples. Their recorded pre-slips lasted on the order of 10 seconds at slip speeds up to about
203 0.4 μm/s before they transitioned into unstable dynamic ruptures.

204 Our spatial and temporal resolution is not sufficient to clearly resolve the co-seismic displacement. At the
205 end of the pre-slip phase, the total displacement jumps by 5.5 μm in 0.022 s. It is likely that the total co-
206 seismic displacement was reached after a much shorter time and the slip velocity was >250 μm/s. The fast
207 coseismic slip transitioned into afterslip with a much lower slip velocity. We model the afterslip using
208 the model proposed in Marone et al. (1991). They provide a closed form solution for the expected
209 afterslip of an earthquake based on rate-and-state friction theory assuming an earthquake that propagates
210 into a velocity-strengthening region and resulting from relaxation of the stress perturbation. It is given by

211 $U_p = \frac{a-b}{k} ln\left[\left(\frac{kV_{CS}}{a-b}\right)t + 1\right] + V_0 t$, where *a-b* is the friction rate parameter, *k* is the thickness-averaged
212 stiffness, V_0 is the pre-seismic slip speed, V_{CS} is the thickness-averaged coseismic slip velocity within the
213 velocity strengthening region and *t* is time. This can be rewritten as

214    $U_p = \alpha \ln \left[\frac{V_{CS}}{\alpha} t + 1\right] + V_0 t$, with $\alpha = \frac{a-b}{k}$. A good fit is achieved for $\alpha = 1.5 \cdot 10^{-6}$ m, $V_{CS} = 2.5 \cdot$

215   10^{-4} m/s and $V_0 = 1.2 \cdot 10^{-6}$ m/s (Figure 3a). The pre-seismic slip speed V_0 does correspond to the inter-

216   seismic creep measured for fault systems. This value should be negligible in our case since a 13.4 MPa

217   stress change was required to initiate rupture. However, to achieve a good fit during the later period of the

218   afterslip phase, a similar parameter is required. We hypothesize that the continuously increasing pressure

219   (from 13.3 to 14 MPa) during the 3 second slip event may have modulated afterslip and caused this linear

220   component of the deformation transient. Further, we highlight that the recorded displacement transient

221   shares functional behavior with constitutive equations for creep and stress relaxation for bulk rock

222   materials of a wide range of lithologies (Main, 2000; Perfettini & Avouac, 2004; Sone & Zoback, 2013).

223   We do not see a deviation of the pressure transient from a linear increase during the slip event. Given an

224   upper bound for the crack opening of 5 μm and a fracture area of 1 m^2, an additional volume of up to 5 μL

225   could have been created. In the 3 second time frame of the slip event, the fluid increment from the

226   ongoing injection was 10 mL, which is much larger than what could possibly leak-off into the reactivated

227   fracture. Hence the measured injection pressure could not have been perturbed by the slip event.

228

Conclusions

230   Before opening a hydraulic fracture, we observed shear reactivation of a preexisting weakness associated

231   with a seismic event. The obtained location and activation pressure are consistent with slip on a foliation

232   plane. Additional pressurization in the first and subsequent injections could not reactivate this slip patch

233   further. No other episodic displacements were measured that could be tied to discrete events.

234   For the first time, we directly observed co-seismic deformation including the three phases of shear slip

235   that were previously only observed separately or were only predicted by numerical models. Of the total

236   accumulated slip about 30% occurred as pre-slip, 25% occurred co-seismically, leading to recorded

237   seismic waves, and 45% occurred as transient afterslip. The observed pre-slip demonstrates stable sliding

238   conditions leading into fast co-seismic slip. Slip was arrested over a three second period of afterslip. No

239   further reactivation of this fracture was observed later when hydraulic fracturing conditions were

240   achieved, indicating a total stress drop of the slip patch.

241   The activated orientation is also very active in later stimulations as shown in Schoenball et al. (2020).

242   This indicates that rock fabric such as bedding and foliation planes may play a bigger role in hydraulic

243   stimulations than previously thought.

244

Appendix 1: EGS Collab Team

J. Ajo-Franklin[1,2], T. Baumgartner[3], K. Beckers[4], D. Blankenship[5], A. Bonneville[6], L. Boyd[7], S. Brown[8], J.A. Burghardt[6], C. Chai[9], A. Chakravarty[1], T. Chen[10], Y. Chen[10], B. Chi[2], K. Condon[11], P.J. Cook[1], D. Crandall[8], P.F. Dobson[1], T. Doe[12], C.A. Doughty[1], D. Elsworth[13], J. Feldman[5], Z. Feng[10], A. Foris[5], L.P. Frash[10], Z. Frone[7], P. Fu[14], K. Gao[10], A. Ghassemi[15], Y. Guglielmi[1], B. Haimson[11], A. Hawkins[16], J. Heise[3], C. Hopp[1], M. Horn[3], R.N. Horne[16], J. Horner[6], M. Hu[1], H. Huang[17], L. Huang[10], K.J. Im[13], M. Ingraham[5], E. Jafarov[10], R.S. Jayne[1], T.C. Johnson[6], S.E. Johnson[1], B. Johnston[4], S. Karra[10], K. Kim[1], D.K. King[5], T. Kneafsey[1], H. Knox[6], J. Knox[6], D. Kumar[15], K. Kutun[18], M. Lee[5], K. Li[16], Z. Li[13], M. Maceira[9], P. Mackey[8], N. Makedonska[10], C.J. Marone[13], E. Mattson[19], M.W. McClure[20], J. McLennan[21], T. McLing[17], C. Medler[22], R.J. Mellors[14], E. Metcalfe[7], J. Miskimins[18], J. Moore[8], C.E. Morency[14], J.P. Morris[14], T. Myers[5], S. Nakagawa[1], G. Neupane[17], G. Newman[1], A. Nieto[7], T. Paronish[8], R. Pawar[10], P. Petrov[1], B. Pietzyk[3], R. Podgorney[17], Y. Polsky[9], J. Pope[5], S. Porse[7], J.C. Primo[1], C. Reimers[22], B.Q. Roberts[6], M. Robertson[1], V. Rodriguez-Tribaldos[1], W. Roggenthen[22], J. Rutqvist[1], D. Rynders[3], M. Schoenball[1], P. Schwering[5], V. Sesetty[15], C.S. Sherman[14], A. Singh[16], M.M. Smith[14], H. Sone[11], E.L. Sonnenthal[1], F.A. Soom[1], D.P. Sprinkle[6], S. Sprinkle[1], C.E. Strickland[6], J. Su[5], D. Templeton[14], J.N. Thomle[6], C. Ulrich[1], N. Uzunlar[22], A. Vachaparampil[15], C.A. Valladao[1], W. Vandermeer[7], G. Vandine[3], D. Vardiman[3], V.R. Vermeul[6], J.L. Wagoner[14], H.F. Wang[11], J. Weers[4], N. Welch[10], J. White, M.D. White[6], P. Winterfeld[18], T. Wood[1], S. Workman[8], H. Wu[14], Y.S. Wu[18], E.C. Yildirim[13], Y. Zhang[16], Y.Q. Zhang[1], Q. Zhou[1], M.D. Zoback[16]

[1] Lawrence Berkeley National Laboratory, [2] Rice University, [3] Sanford Underground Research Facility, [4] National Renewable Energy Laboratory, [5] Sandia National Laboratories, [6] Pacific Northwest National Laboratory, [7] U.S. Department of Energy, [8] National Energy Technology Laboratory, [9] Oak Ridge National Laboratory, [10] Los Alamos National Laboratory, [11] University of Wisconsin-Madison, [12] TDoeGeo Rock Fracture Consulting; Golder Associates Inc, [13] Pennsylvania State University, [14] Lawrence Livermore National Laboratory, [15] The University of Oklahoma, [16] Stanford University, [17] Idaho National Laboratory, [18] Colorado School of Mines, [19] Mattson Hydrology LLC, [20] ResFrac, [21] University of Utah, [22] South Dakota School of Mines and Technology

Acknowledgements

283

Data Availability Statement

285 The data presented in this manuscript can be accessed from the Geothermal Data Repository at
286 https://gdr.openei.org/submissions/1289.

287

References

289 Cattania, C., & Segall, P. (2020). Precursory slow slip and foreshocks on rough faults. *EarthArXiv*
290 *Preprints*, doi:10.31223/osf.io/9xphk

291 Chai, C., Maceira, M., Santos-Villalobos, H.J., Venkatakrishnan, S.V., Schoenball, M., Zhu, W., Beroza,
292 G.C., Thurber, C., EGS Collab Team (2020). Using a Deep Neural Network and Transfer Learning to
293 Bridge Scales for Seismic Phase Picking. *Geophys. Res. Lett.*, doi:10.1029/2020GL088651

294 Ellsworth, W. L., & Beroza, G. C. (1995). Seismic Evidence for an Earthquake Nucleation Phase.
295 *Science*, *268*(5212), 851–855. https://doi.org/10.1126/science.268.5212.851

296 Ellsworth, W. L., & Bulut, F. (2018). Nucleation of the 1999 Izmit earthquake by a triggered cascade of
297 foreshocks. *Nature Geoscience*, *11*(7), 531–535. https://doi.org/10.1038/s41561-018-0145-1

298 Heise, J. (2015). The Sanford Underground Research Facility at Homestake. Journal of Physics:
299 Conference Series, v. 606 (1), *IOP Publishing*, 25 p., doi:10.1088/1742-6596/606/1/012015

300 Guglielmi, Y., Cappa, F., Lançon, H., Janowcsyk, J. B., Rutqvist, J., Tsang, C.-F., & Wang, J. S. Y.
301 (2014). ISRM Suggested Method for Step-Rate Injection Method for Fracture In-Situ Properties
302 (SIMFIP): Using a 3-Components Borehole Deformation Sensor. *Rock Mechanics and Rock Engineering*,
303 *47*(1), 303–311. https://doi.org/10.1007/s00603-013-0517-1

304 Guglielmi, Y., Cook, P., Soom, F., Schoenball, M., Dobson, P., & Kneafsey, T. (2021). In situ continuous
305 monitoring of borehole displacements induced by stimulated hydrofracture growth. *Geophysical Research*
306 *Letters*, 48, e2020GL090782. https://doi.org/10.1029/2020GL090782

307 Kneafsey, T. J., Blankenship, D., Knox, H. A., Johnson, T. C., Ajo-Franklin, J. B., Schwering, P. C., et al.
308 (2019). EGS Collab Project: Status and Progress. In *Proceedings 44th Workshop on Geothermal Reservoir*
309 *Engineering, Stanford University*, 16 p.

310 Kneafsey, T. J., Blankenship, D., Dobson, P. F., Morris, J. P., White, M. D., Fu, P., et al. (2020). The
311 EGS Collab Project: Learnings from Experiment 1. In *Proceedings 45th Workshop on Geothermal*
312 *Reservoir Engineering*, 15 p., Stanford University, Stanford, California.

313 Kneafsey, T., Blankenship, D., Dobson, P., White, M., Morris, J.P., Fu, P., Wu, H., Schwering, P.C., et al.
314 (2021). Fracture stimulation and chilled-water circulation through deep crystalline rock: Characterization,
315 modeling, monitoring, and heat-transfer assessment. In *Proceedings, 46th Workshop on Geothermal*
316 *Reservoir Engineering*, Stanford University, Stanford, California.

317 Kwiatek, G., Plenkers, K., Dresen, G., JAGUARS Research Group (2011) Source Parameters of
318 Picoseismicity Recorded at Mponeng Deep Gold Mine, South Africa: Implications for Scaling Relations.
319 *Bulletin of the Seismological Society of America*; 101 (6): 2592–2608. doi:
320 https://doi.org/10.1785/0120110094

321 Main, I. G. (2000). A damage mechanics model for power-law creep and earthquake aftershock and
322 foreshock sequences. *Geophysical Journal International*, 142(1), 151–161.
323 https://doi.org/10.1046/j.1365-246x.2000.00136.x

324 Marone, C. J., Scholtz, C. H., & Bilham, R. (1991). On the mechanics of earthquake afterslip. *Journal of*
325 *Geophysical Research*, 96(B5), 8441. https://doi.org/10.1029/91JB00275

326 McLaskey, G. C., & Lockner, D. A. (2014). Preslip and cascade processes initiating laboratory stick slip.
327 *Journal of Geophysical Research: Solid Earth*, 119(8), 6323–6336.
328 https://doi.org/10.1002/2014JB011220

329 McLaskey, G. C. (2019). Earthquake Initiation from Laboratory Observations and Implications for
330 Foreshocks. *Journal of Geophysical Research: Solid Earth*, 124(12), 12882–12904.
331 https://doi.org/10.1029/2019JB018363

332 McGuire, J. J., Boettcher, M. S., & Jordan, T. H. (2005). Foreshock sequences and short-term earthquake
333 predictability on East Pacific Rise transform faults. *Nature*, 434(7032), 457–461.
334 https://doi.org/10.1038/nature03377

335 Nadeau, R. M., & Johnson, L. R. (1998). Seismological studies at Parkfield VI: Moment release rates and
336 estimates of source parameters for small repeating earthquakes. *Bulletin of the Seismological Society of*
337 *America*, 88(3), 790–814.

338 Perfettini, H., & Avouac, J.-P. (2004). Postseismic relaxation driven by brittle creep: A possible
339 mechanism to reconcile geodetic measurements and the decay rate of aftershocks, application to the Chi-
340 Chi earthquake, Taiwan. *Journal of Geophysical Research: Solid Earth*, 109(B2).
341 https://doi.org/10.1029/2003JB002488

342 Savage, H. M., Kirkpatrick, J. D., Mori, J. J., Brodsky, E. E., Ellsworth, W. L., Carpenter, B. M., et al.
343 (2017). Scientific Exploration of Induced SeisMicity and Stress (SEISMS). *Scientific Drilling*, 23, 57–63.
344 https://doi.org/10.5194/sd-23-57-2017
345 Schoenball, M., Baujard, C., Kohl, T., & Dorbath, L. (2012). The role of triggering by static stress
346 transfer during geothermal reservoir stimulation. *Journal of Geophysical Research*, 117(B9), B09307.
347 https://doi.org/10.1029/2012jb009304
348 Schoenball, M., Ajo-Franklin, J. B., Blankenship, D., Chai, C., Chakravarty, A., Dobson, P., et al. (2020).
349 Creation of a mixed-mode fracture network at mesoscale through hydraulic fracturing and shear stimulation.
350 *Journal of Geophysical Research: Solid Earth*, 125, e2020JB019807. https://doi.org/10.1029/2020JB019807
351 Sone, H., & Zoback, M. D. (2013). Mechanical properties of shale-gas reservoir rocks — Part 2: Ductile
352 creep, brittle strength, and their relation to the elastic modulus. *GEOPHYSICS*, 78(5), D393–D402.
353 https://doi.org/10.1190/geo2013-0051.1
354 Tape, C., Holtkamp, S., Silwal, V., Hawthorne, J., Kaneko, Y., Ampuero, J. P., et al. (2018). Earthquake
355 nucleation and fault slip complexity in the lower crust of central Alaska. *Nature Geoscience*, *11*(7), 536–
356 541. https://doi.org/10.1038/s41561-018-0144-2
357 Yoon, C. E., Yoshimitsu, N., Ellsworth, W. L., & Beroza, G. C. (2019). Foreshocks and Mainshock
358 Nucleation of the 1999 M w 7.1 Hector Mine, California, Earthquake. *Journal of Geophysical Research:*
359 *Solid Earth*, *124*(2), 1569–1582. doi:10.1029/2018JB016383

Geophysical Research Letters

Supporting Information for

In-situ observation of pre-, co- and post-seismic shear slip at 1.5 km depth

Martin Schoenball[1,*], Yves Guglielmi[1], Jonathan B. Ajo-Franklin[2], Paul Cook[1], Patrick F. Dobson[1], Chet Hopp[1], Timothy J. Kneafsey[1], Florian Soom[1], Craig Ulrich and EGS Collab Team

[1] Lawrence Berkeley National Laboratory, [2] Rice University, [*] now at Nagra

Contents of this file

Detection of Seismic Events

The sensors were grouted in place in six monitoring boreholes, surrounding the experimental volume in 3-D. Most events that occurred during the fracture initiation are too weak to determine reliable phase arrivals and locate the hypocenters. Hence, for this study we focus on event detection rather than location. We use detected events as a proxy for fracturing activity. The results of the passive seismic monitoring of a larger series of hydraulic stimulations are described in detail in Schoenball et al. (2020). For event detection we use an STA/LTA detector and require a detection on all three components of the accelerometer OT16. The selected sensor is the second closest accelerometer to the stimulated interval (d = 11.2 m) and has a very good coupling to the host rock. It is much more sensitive to the early seismic activity than any other sensor. In fact, most events are only visible on the channels of this sensor. For quality control we manually confirmed a random sample of detected events to be indeed seismic events.

Hydraulic fracture initiation and propagation

Concomitant with the departure from the linear pressure regime, we begin to see seismic activity and significant displacements accumulating in the pressurized interval (Figure S1). Displacements started out to be in shear before we observed borehole-axial deformation. The recorded axial displacements are negative, indicating that an opening

mode fracture was located in the pressurized interval but outside of the SIMFIP sensor clamps. Indeed, the negative displacements correspond to the compression of the rock between the SIMFIP clamping points as the hydraulic fracture opened in the adjacent rock between one clamping point and a packer element.
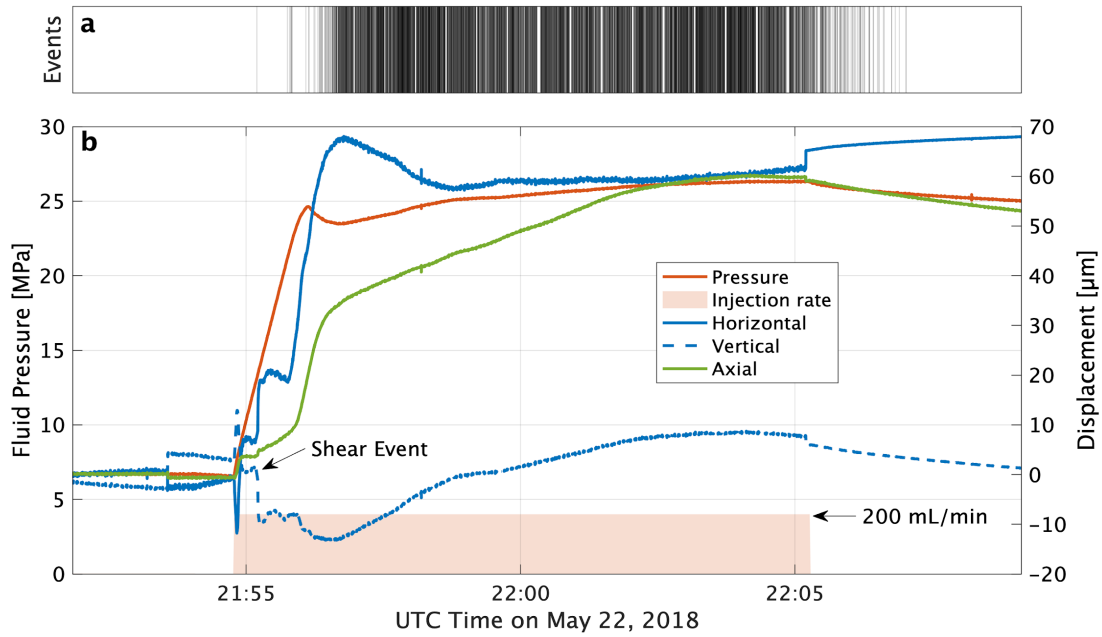

Figure S1. (a) Occurrence times of seismic events detected on accelerometer OT16. (b) Injection rate and pressure (orange) and the displacements recorded by the SIMFIP probe in the two radial directions (blue) and axial (green).
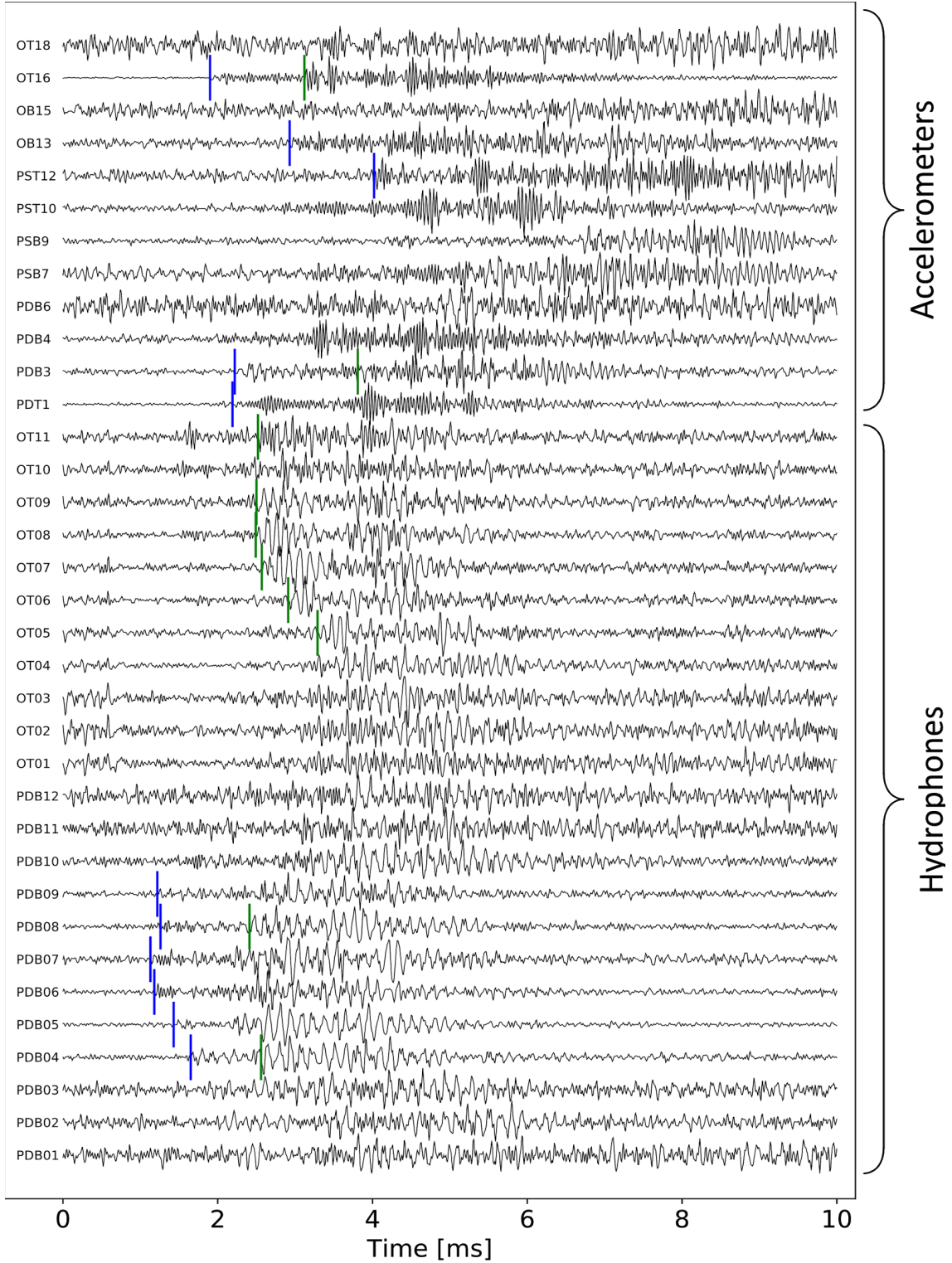
Figure S2. Waveforms of the shear event recorded on accelerometers (only x-components shown) and hydrophones. Manually picked P and S-wave arrivals are marked by blue and green dashes, respectively.